Finite Element Modeling of Indentation Behavior of Dual Phase Steels: Role of Plastic Zone Size in Property Mapping

SOUDIP BASU,[1] NIDHIN G. MATHEWS,[1] TEJAS S. CHAUDHARI,[1] and B. NAGAMANI JAYA (iD)[1,2]

1.—Department of Metallurgical Engineering and Materials Science, IIT Bombay, Powai, Mumbai 400076, India. 2.—e-mail: jaya86@gmail.com

Instrumented indentation is gaining ground as a tool for generating mechanical phase maps in composite structures such as dual phase (DP) steels. The plastic zone evolution dictates the indentation parameters in such measurements and needs to be estimated accurately. This study uses finite element modeling to simulate nanoindentation responses on a ferrite–martensite DP steel to directly quantify the plastic zone in the heterogeneous microstructure. The polycrystalline tensile deformation response of individual phases of the composite structure are fed as input to a micro-mechanical finite element model to determine the indentation response. The effect of extrinsic parameters, such as tip radius and geometry, and intrinsic microstructural parameters, like the martensite volume fraction and hardness on the plastic zone evolution and the hardness derived thereof, is established. The model correctly predicts the trend in hardness of individual phases as well as the two-phase composite structure. More importantly, it allows for direct visualization of the plastic zone and the stress triaxiality underneath the complex stress state, enabling prediction of failure modes in these microstructures. This offers a complementary tool to the expensive process of locating and cross-sectioning the indents through site-specific micromachining tools to assess the damage zone under them.

INTRODUCTION

Depth-sensing indentation, also known as instrumented indentation, is a widely used tool to extract local, site-specific mechanical properties of materials in small volumes, which eliminate the need to image the indents.[1] Since the pioneering work of Oliver–Pharr,[2] several modifications of the technique have been used to determine the elastic modulus and hardness from indentation load–depth curves[3–5] in complex material systems, including multilayers, multi-phase composites, and thin films. There are obvious advantages in being able to quantify the actual plastic zone evolution during indentation, especially in mechanical phase maps of heterogeneous, complex microstructures.[6–8] However, imaging the actual plastic zone size (PZS) is challenging

and expensive. Multi-scale finite element modeling (FEM) and simulation of indentation behavior through both continuum and crystal plasticity-based models have been able to provide this complementarity to experiments.[9–11] For example, Yan et al. showed how virtual imaging of simulated indentation areas could correct for pile-up and sink-in effects, especially in particle-reinforced composites.[12]

Estimation of the PZS via analytical models or finite element simulations has been pursued by various researchers. Mechanistically, the average pressure translates to the physical property, hardness, when the plastic zone grows into a hemispherical cavity and extends to the surface. Using Johnson's expanding cavity model,[13] the PZS, c around indents in elastic–perfectly plastic solids is given by[14–18]:

$$\left(\frac{c}{a}\right)^3 = \frac{E \tan\beta}{6(1-v)\sigma_{ys}} + \frac{2(1-2v)}{3(1-v)} \qquad (1)$$

where a is the contact radius, E is the Young's modulus, v is the Poisson's ratio, σ_{ys} is the yield strength, $\beta = \pi/2 - \theta$ is the inclination of the indenter face to the surface of the solid, and θ is the semi-angle of the conical indenter. While integral–form relationships between the internal pressure and the PZS have been developed,[19–23] Mata et al.[24] provided a closed-form solution of the PZS in elastic–perfectly plastic as well as strain-hardening solids for axisymmetric indenters. For elastic–perfectly plastic solids, it is given by:

$$\frac{c}{R} = \frac{z_{ys} + 1.217a_s}{a_s/0.635} = \left(\frac{2E}{3\sigma_{ys}}\right)^{1/3} \qquad (2)$$

where z_{ys} is the plastic zone depth, $R = \frac{a_s}{0.635}$ is the radius of the equivalent spherical indenter tangent to the contact point like that of a conical indenter with a half-cone angle 70.3°, also called the cavity radius, and a_s is the contact radius. For strain-hardening materials, their finite element simulations showed an outward spread of the plastic zone with increasing strain-hardening exponent (n) for a fixed E and σ_{ys}. They provided a fitting function that also describes the plastic zone for those cases. Using FEM, Chen and Bull[25,26] established and validated the following relationship between PZS and indentation depth in elastic–perfectly plastic materials with an H/E ratio < 0.35:

$$\frac{R_p}{\delta_m} = -12.907\frac{H}{E_r} + 4.5451 \qquad (3)$$

where R_p is the radius of the plastic zone, δ_m is the maximum indentation depth, H is the hardness, and E_r is the reduced elastic modulus. This relationship is primarily applicable for ceramics indented using conical tips and accounts for tip-rounding effects. All these models assume an isotropic homogeneous material in their calculations, and the majority were developed to determine the depth of penetration in thin films and coated systems in order to avoid substrate effects.

While the above authors used mathematical models to describe the plastic zone underneath the indenters, there are several others who validated these models using direct experimental observations and described the actual mechanism of plastic zone evolution. Nix and Gao[27–29] assumed the plastic zone to be a hemisphere containing circular loops of geometrically necessary dislocations (GNDs). This microstructural assumption allowed the accommodation of a strain gradient (tan (β/α)) and the development of a strain gradient plasticity theory that accurately captured the indentation size effect in metals.[29] Experimentally, the high spatial resolution of X-ray micro-diffraction was used to reveal the lattice rotations (evidenced in the form of streaking of the Laue spots) from the plastic zones of indentations in (111) copper.[30,31] The magnitude of streaking of the Laue spots was found to be independent of the indentation depth, indicative of constant total lattice rotation and effective indentation strain, which is consistent with the assumptions of the Nix–Gao model.[29] In contrast, through a combination of focused ion beam (FIB) cross-sectioning and electron backscattered diffraction (EBSD), it was shown that lattice misorientation angles (ω) increased with increasing depth underneath indentations of varying loads.[32,33] Since ω is directly proportional to the GND density,[34,35] the increase in ω with increasing depth is in contradiction to the Nix–Gao model.[29]

The PZS dictates the minimum distance that has to be maintained between indents to ensure zero or negligible mutual interaction, and is hereafter referred to as indent spacing. The indent spacing becomes especially important during high-speed nanoindentation which offers a possibility for obtaining high-throughput data like phase mapping and the ability to detect microstructural (dislocation density) changes, such as during recovery, recrystallization, and deformation.[36] Hintsala et al.,[37] in their review of the effect of indent spacing, loading rates, and pile-up or sink-in during nanoindentation mapping, showed the effect of overlapping plastic zones on the hardness and modulus of single-crystal aluminium. Li et al.[38] studied the extraction of pop-in statistics from a microstructural perspective, and elucidated the dependence of the indent spacing on Peierls–Nabarro stress, elastic constants, and dislocation density of the material. Phani et al.[39] used a combination of high-speed nanoindentation mapping and FEM to show that a minimum indent spacing of 10 times the indentation depth (in contrast to the well-known 20 times[40,41]) resulted in negligible deviation in hardness for a myriad of bulk materials. This study mainly involved single-phase materials and hence does not take into account phase-wise variation in properties and PZS.

The ability to predict the PZS and shape in multi-phase composites enables revised and realistic thumb rules on the distance between indents for high-throughput hardness mapping experiments. A few groups have pursued a combination of finite element simulations and nanoindentation tests to determine various parameters influencing the indentation behavior of dual-phase (DP) steels. Matsuno et al. placed indentations on ferrite at various distances from the ferrite–martensite interface of a DP steel to determine the critical distance at which the influence of the second phase impacted the plastic zone and hardness measurement of the ferrite.[42] They reported this distance to be ~1 μm, below which the hardness of the ferrite phase begins to increase, due to the influence of the hard martensite. However, the relative distance with respect to the size of the feature as well the depth of indentation were not explicitly analyzed in their work. Kadkhodapour et al.[43] also showed such an influence in the hardening behavior of ferrite when measured in close proximity to martensite. The

critical distance from the interphase boundary in their case was, however, found to be higher, at 3 μm, which may be due to the difference in the size of the features in this study compared to Matsuno et al.[42] They attribute this to local hardening in the ferrite due to GNDs prior to the indentation process. Again, the depth of indentation and its effect was not systematically studied. In heterogeneous systems of this nature with different strain-hardening behaviors of the individual phases, the plastic zone cannot be assumed to be a hemispherical cavity. The simulation of the indentation response in such materials also helps to quantify the stresses and triaxiality underneath the indenter as a function of second phase size, shape, and volume fraction, and as a function of tip geometry, which helps to predict the damage and failure mode under indentation stress fields. They are also important as inputs for integrated computational materials engineering efforts. This study is a demonstration of these applications on a ferrite (α)–martensite (α') DP steel, which can be considered to be a composite with a soft ferrite matrix reinforced by hard martensite islands.

Previous studies have focused on determining the properties of ferrite in close proximity to martensite islands. However, the edge effects will not be the same for hardness measurements of martensite, surrounded by the soft ferrite phase, and these critical relative spacings will need to be different. In our previous study,[44] tempering was used to reduce the relative difference in hardness between the two phases, but their effect on PZS evolution is not known. In the present study, FEM simulations are carried out to determine the maximum depth of indents on the martensite islands, such that an unambiguous mechanical phase mapping becomes possible for various thermo-mechanically processed microstructures of DP steel, while being able to separate out the interface effects. Our model is only a first approximation of the properties, considering both ferrite and martensite as polycrystalline aggregates, constituting a two-phase composite. The focus is primarily on the α', which typically forms equiaxed or irregularly shaped islands in the α matrix.

This paper is organised as follows. The methodology of finite element simulations emulating the experimental measurements using different indenter tips are described first. This is followed by the results section, which starts with an experimental verification of the simulated hardness measurements on individual phases α, α', and the interface, and determination of critical normalized indentation depth to distance from the interphase boundary essential to extract properties of the α'. More detailed calculations of PZS for various tip geometries and radii follow in order to offer a choice to the user based on the α' feature size in the microstructure. Further the effect of thermo-mechanical process parameters, especially tempering, captured in

terms of yield strength and strain-hardening behavior as inputs on the hardness, is determined. Finally, the composite microstructure with changing volume fraction and hardness differentials, emulating a realistic microstructure, is indented using simulations to predict their hardness, and compared to experimentally determined values. A discussion on the advantages and limitations of FEM as a complementary technique to experimental measurements of plastic zone is presented before concluding the work.

METHODOLOGY

Material

DP steels are advanced high-strength steels containing martensitic islands in a ferritic matrix. The martensite islands nucleate from prior austenite grain boundaries during inter-critical annealing followed by quenching, and form the hard reinforcing phase in the soft ductile ferritic matrix. It has been found that the volume fraction of α' and the hardness differential $\Delta H = H_{\alpha'}$-H_α (where H refers to the hardness of the corresponding phase) are the two most important factors that govern the strain partitioning and control the damage initiation and failure in these materials.[45] The typical microstructure of DP steels considered here consists of α with a grain size of 2.5 ± 1.7 μm and α' islands of varying shape and size, ranging upwards from 3.0 ± 2.0 μm (Fig. 1a, c). The scatter bands represent standard deviations in the average grain-size of the ferrite and the colony size of martensite measured via EBSD maps of DP steel. Based on the strength requirement, the volume fraction of α' typically ranges between 10% and 30% and, based on the carbon content, the ΔH ranges from 5.4 GPa to $\sim$1.1 GPa. In the DP 600 shown in Fig. 1(a), the volume fraction of α' is $\sim$10% with a ΔH of 5.4 GPa, as measured from nanoindentation experiments.[44] The indents for these measurements were placed in an array at a distance of 10 μm, based on the present thumb rule of indent spacing being greater than 20 times[40,46] the maximum depth (Fig. 1b). The tempered microstructures were generated by heating the DP 600 at various times and temperatures, details of which can be found elsewhere.[44] The volume fraction of martensite was changed by heating the DP to 1073 K for 15 min followed by water quenching in a Gleeble™ thermo-mechanical simulator.

Experimental Methodology

All the samples were polished to a very low surface roughness (< 50 nm) through sub-micron colloidal silica polishing. EBSD measurements were carried out after the indentation in a FEI™ Quanta-3D field-emission gun dual-beam system with an EDAX-TSL™ EBSD set-up to identify and map the hardness values of the individual phases.
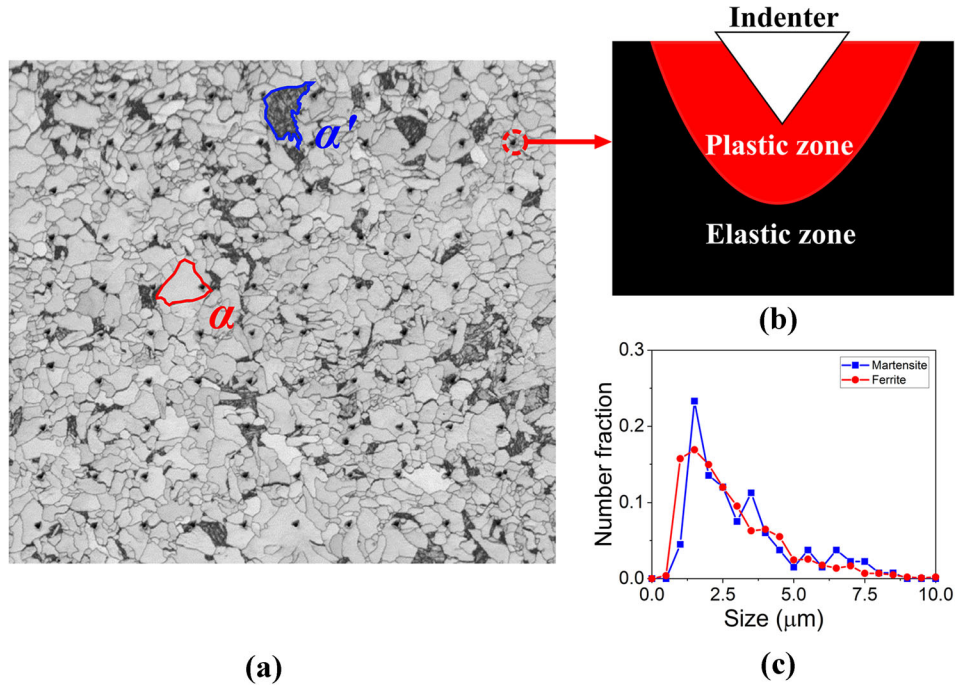
Fig. 1. (a) Image quality (IQ) map of a ferrite (α)–martensite (α') dual phase microstructure with an array of Berkovich indents; an α' island and an α grain have been marked with a blue and red outline, respectively. (b) Schematic of the plastic zone size under an indent in a heterogeneous microstructure (c) Grain size distributions of ferrite and martensite obtained from EBSD (Color figure online).

Hardness tests were carried out at two different length scales. Microhardness tests were carried out in a Vickers indenter at 10 gf maximum load with a dwell time of 10 s, and the hardness is derived using:

$$H = \frac{P}{A} \tag{4}$$

where P is the maximum load and A is the projected contact area given by $\frac{d_{avg}^2}{2}$, d_{avg} being the average diagonal length of the indent measured by optical imaging. A focused ion beam cross-section was milled to reveal the indented region and the associated plastic zone of one such indent.

The nanoindentation measurements were carried out in a Hysitron^{TM} TI Premier nanoindenter with a Berkovich tip in load-controlled mode (maximum load of 4 mN), with a loading and unloading rate of 0.4 mN/s, and dwell time of 5 s. Elastic modulus and hardness values were estimated by the standard Oliver–Pharr method.[2]

Simulation Methodology

Finite element simulations were carried out in ABAQUS/CAE v.6.14-4® with the methodology described in Figs. 2 and 3. An axisymmetric model is used when the entire structure is assumed to be a homogeneous isotropic single phase, and a 3-D model is used when the two-phase polycrystalline aggregate structure is explicitly modeled. Micromechanical models of α matrix with 10, 20, and 30%

α' were created by partitioning the structure with a random distribution of martensite particles in the size range of 0.4–7.0 μm taken as input from experimental sampling (Fig. 2a, b). This is a model idealised from the microstructure shown in Figs. 1a and 2a, assuming all the islands of α' are spherical in shape. Further details of the algorithm are given in the appendix 1. The experimentally measured change in hardness differential as a function of tempering heat treatment for the various microstructures of DP steel are shown in Fig. 2c. Input properties were assigned from the Rodriguez model of tensile deformation response of the two polycrystalline phases,[47] fit to the Holloman equation (Figs. 2d and 3a). This is to account for the contribution of the neighboring grains on the deformation of α or α' even when indented on individual grains. The Rodriguez model is an analytical equation describing the hardening behavior of the phase, including contributions from the Peierl's stress due to solid solution formers (σ_0) and interstitial solute-carbon ($\Delta\sigma$) for ferrite and martensite, and the classic Taylor hardening (due to dislocations in a polycrystalline material) (Eq. 5). The constants of the Taylor hardening term is found by fitting the experimental tensile strength data from a variety of steels, including ferritic, pearlitic, martensitic, and bainitic steels. The final equation from the Rodriguez model used for the fitting is:

$$\sigma = \sigma_0 + \Delta\sigma + \alpha M \mu \sqrt{b} \sqrt{\frac{1 - \exp(-Mk_2\varepsilon)}{k_2 L}} \tag{5}$$
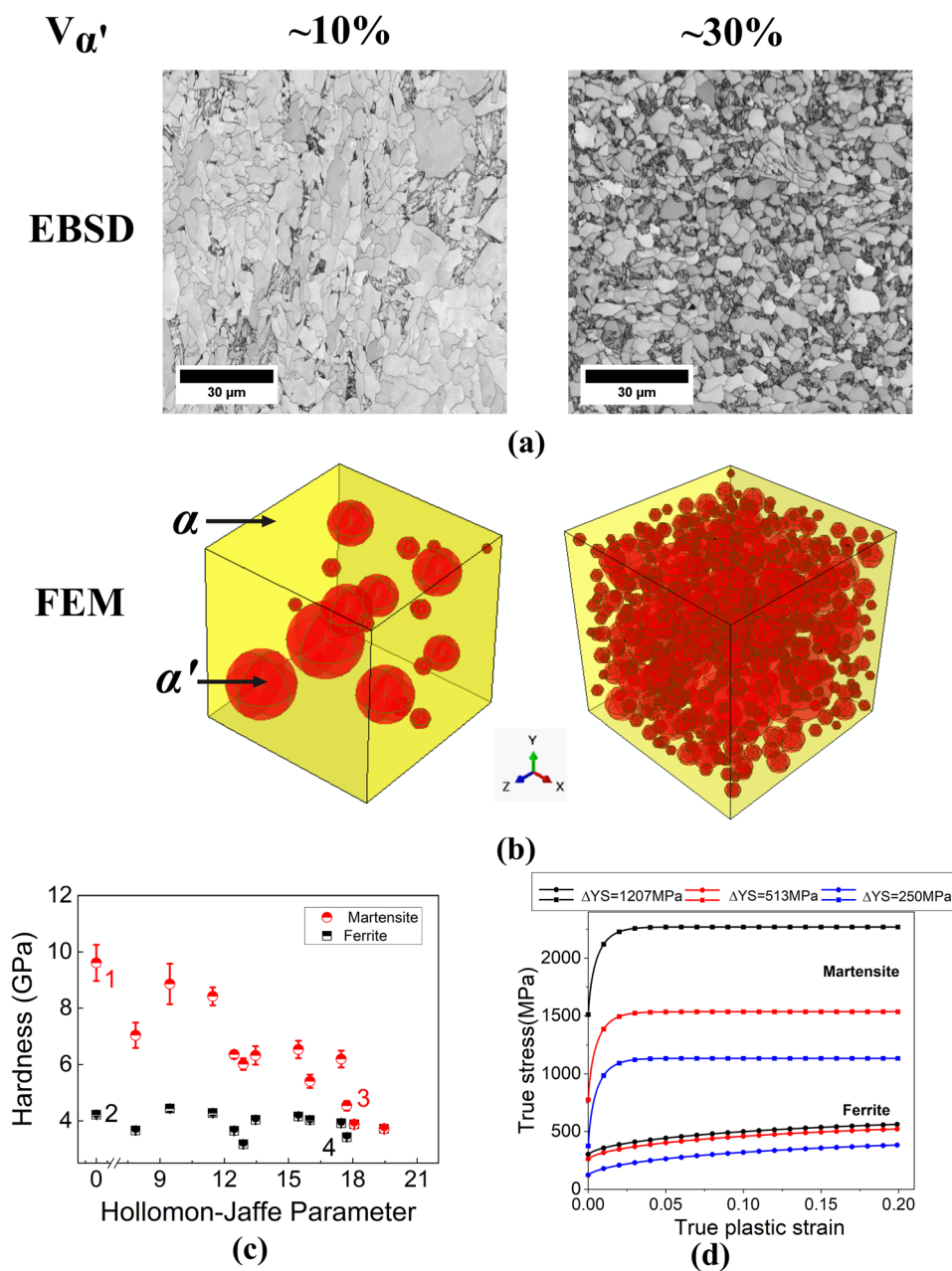
(a)

(b)

(c)

(d)

Fig 2. (a) Image quality (IQ) maps of 10% and 30% martensite microstructures generated via controlled intercritical annealing, and (b) the corresponding micro-mechanical finite element models used to simulate indentation on these structures. (c) Change in ferrite and martensite hardness as a function of increasing intensity of tempering denoted by the Hollomon–Jaffe (temperature–time) parameter (reproduced with permission from Ref 44), (d) model input for parametric simulations of the changing strength differential.

where α is a constant close to 0.33, M is the Taylor factor ($\sim$3), μ is the shear modulus (80 GPa), b is the Burger's vector (0.25 nm), L is the dislocation mean free path, and k_2 is a constant. L values of 8 μm and 0.04 μm were found for ferrite and martensite the respectively, while k_2 values of 1.35 and 40.91 were found for ferrite and martensite the respectively. These values were found by fitting the data to experimental tensile data of a variety of steels, including ferritic and martensitic steels. On using a rule of mixtures for a DP steel with 10% martensite

with the input data obtained from the Rodriguez model, a good correlation was found with the experimentally measured tensile response. Experimental phase-wise hardness data on the DP[44] and the initial yield strength values of DP obtained from the Rodriguez model were fit to a linear equation. This linear relationship was used to interpolate and find the input yield strengths of ferrite and martensite from the experimental phase-wise hardness data of tempered structures. The effects of other microstructural variations in terms of martensite island shape and distribution in ferrite grain size
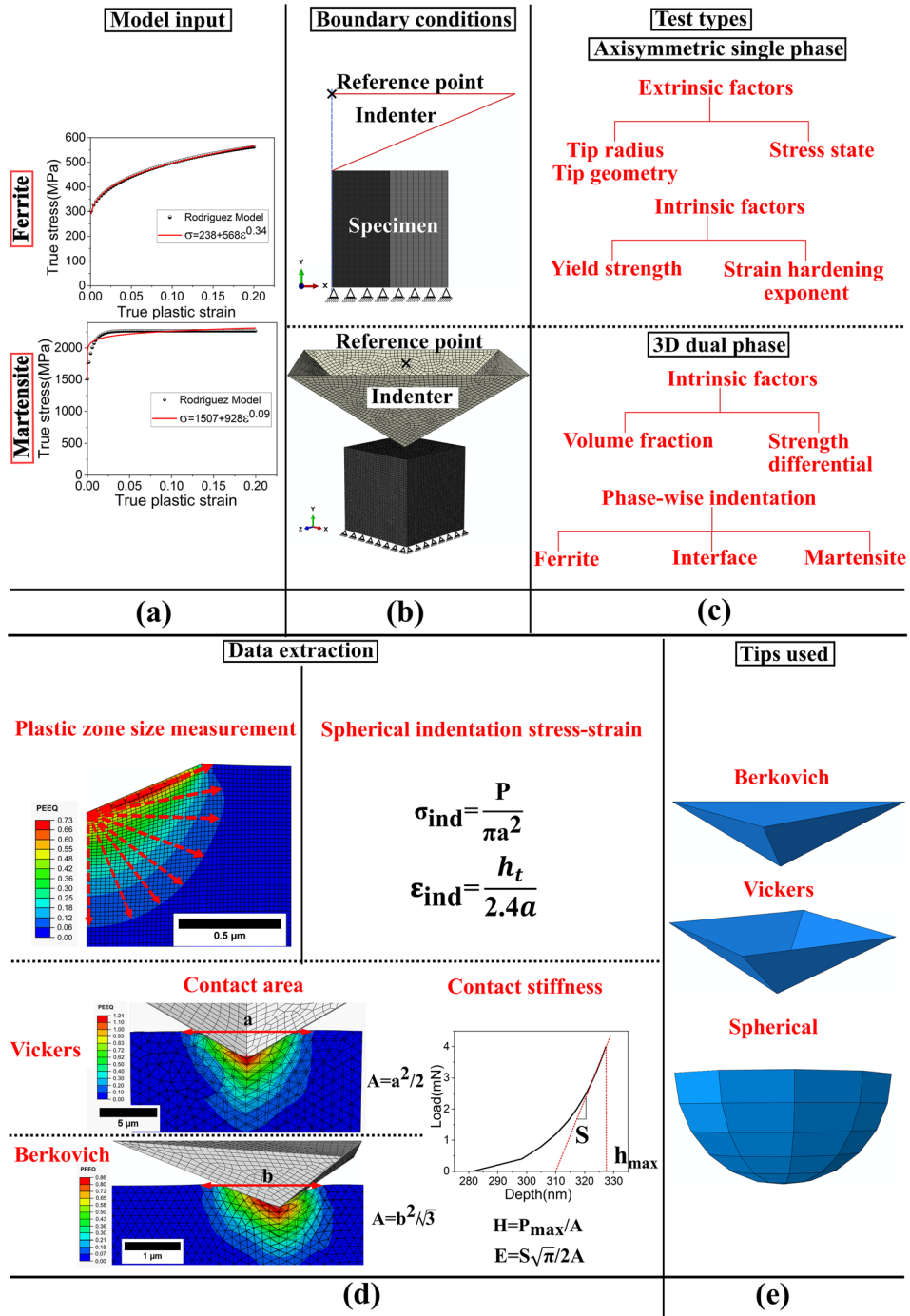
Fig 3. Methodology of the finite element modeling showing: (a) input data for ferrite and martensite. taken from the Rodriguez model [55] plotted along with the corresponding Hollomon equation fit, (b) boundary conditions used, (c) types of tests carried out, (d) data extraction techniques used, and (e) tip types used

were not part of this study. This study does not use grain scale simulations and assumes the entire phase as a polycrystalline entity. However, it can be expanded into a crystal plasticity simulation using orientation-specific grain-level experimental data that are available through micropillar compression tests.[48–52]

Figure 3(a–c) summarizes the input properties, boundary conditions, and variables studied. CAX4R 4-node bilinear type of elements, with a total of 79,200 elements in the axisymmetric model, and, for the 3D model, C3D4 4-node linear tetrahedral type of elements with a total of ~450,000 elements, were used for FEM simulations. For the axisymmetric case, the mesh was refined further within a 3-μm

distance close to the indented region, such that there were at least 50 elements per unit length of α' (Fig. 3(b)). For the 3D model, a maximum mesh size of 0.5 μm was used with adaptive refinement. The mesh size for all simulations near the zone of indentation was 20 nm (which corresponds to a ratio of 0.02 for a 1-μm radius indenter tip). Mesh sensitivity studies were performed, and it was observed that, below a mesh size of 40 nm, a consistent convergent indentation response was obtained.

Pyramidal indenters used were Berkovich and Vickers. Berkovich indenters with an included angle of 142.3° with a sharp point (ideal) and 100 nm radius were used. The Vickers indenter was idealised as sharp and had an included angle of 136°. Berkovich indentation was used to extract the hardness of the individual phases and the interface and compared to experimental nanoindentation measurements, Vickers indentation was used to quantify the hardness of the composite structure to be compared to experimental microhardness measurements. Additionally, spherical indenter tips with radii ranging from 0.1 to 50 μm were used (Fig. 3c) to determine the effect of tip radius on the PZSs. The simulated indentation load (P) – depth (h) response was extracted as output from the reference point of the indenter. For measurement of the PZS in the axisymmetric model, an average of the distances from the point of indentation to the boundary of the finite equivalent plastic strain (PEEQ) contour (beyond which yield criteria are not met) at 7 different angles with 15° step size were taken (Fig. 3d). 3D simulations were carried out with Vickers and Berkovich indenters. Vickers indentations covered multiple phases analogous to a microhardness test, while Berkovich indentations were confined to individual phases analogous to a nanoindentation test. To measure the contact area, the indented surfaces were further sectioned at 90° to the surface. The sectioning plane was along the diagonal and altitude of the indents for the Vickers and Berkovich indents, respectively. The distance from one boundary of the plastic zone (beyond which PEEQ is zero) to the other is measured on the cross-sectioned view of the indent as the contact radii 'a' and 'b' for the Vickers and Berkovich, respectively (Fig. 3d) to account for the pile-up or sink-in which occurs within the plastic zone. These were used to compute the projected contact area according to Eqs. 6 and 7, using the known geometrical relationships.

For the Vickers ($A_{VICKERS}$) indents:

$$A_{VICKERS} = \frac{a^2}{2} \quad (6)$$

where a is the diagonal length of the squared shaped impression.

For the Berkovich (A_{BERK}) indents:

$$A_{BERK} = \frac{b^2}{\sqrt{3}} \quad (7)$$

where b is the altitude of the triangular impression.

Further, adopting Sneddon's criteria for conical indenters (Eq. 8),[53,54] the contact stiffness (S) was found by fitting the first 10% of the unloading response with a linear equation ($P = Sh + C$), where P is the load, h is the indentation depth and C is a constant:

$$P = \alpha h^m \quad (8)$$

where $m = 2$ for conical indenters. Hence, $\frac{dP}{dh} = 2\alpha h$. Therefore, a linear fit to the unloading response is used.

Then, Eq. 9 is used to obtain the elastic modulus:

$$E = \frac{S\sqrt{\pi}}{2\sqrt{A}} \quad (9)$$

RESULTS

### Hardness Measurements through Berkovich Indentations on Individual Phases

Figure 4a shows the load-controlled indents carried out on the ferrite phase, interface and the martensite phase (marked as "Martensite1" in Fig. 4a) of a micro-mechanical model of a DP steel with 10% α' at a peak load of 4 mN. The placement of the indents on ferrite and martensite was meant to ensure no interference from the other phase, as explained later. The hardness obtained using Eqs. 4, 6, and 7 is compared to the experimentally measured values using the Oliver–Pharr method in Fig. 4b at the same load. The trend is very well captured from the simulated data, although there are differences in the actual values. This is obvious from the differences in the simulated and experimental load–depth curves shown in Fig. 4c–e for the three locations. While the loading parts of the curves are quite different, the unloading slopes obtained from them are similar. The difference in plastic depth between experimentally measured and simulated curves implies that the P–h curves from the simulations cannot be used to estimate the contact depth or contact area. However, the ability to visually measure the simulated PZS (Fig. 4f) helps to overcome this, by direct measurement of the deformed area underneath the indent. Therefore, the contact stiffness is used from the simulated P–h response and the projected contact area is directly measured from the PEEQ contours below the indented area. This yields the elastic modulus as 160 GPa for α and 189 GPa for α' (obtained from Eq. 4), which is within reasonable limits of those obtained directly from experiments using the Oliver–Pharr method for α (157.6 GPa $\pm$ 9.6 GPa) and α'(176.1 GPa $\pm$ 11.9 GPa). The hard α' shows a lower
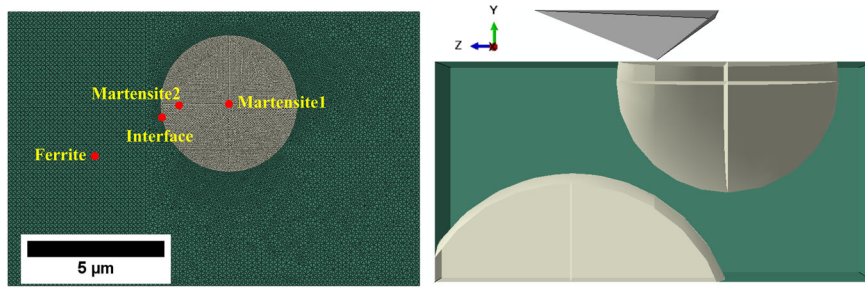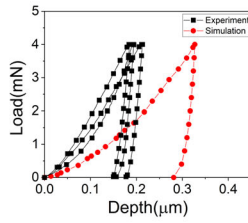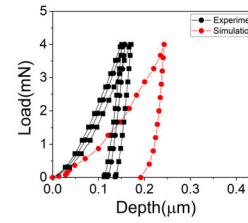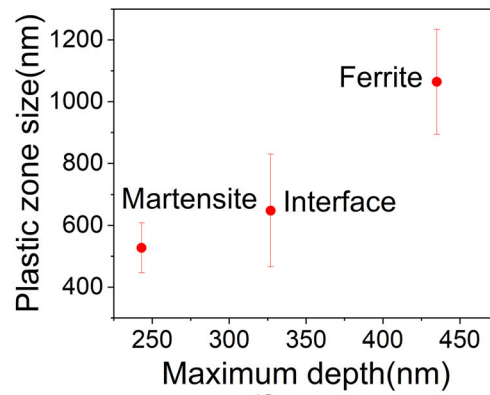
(a)
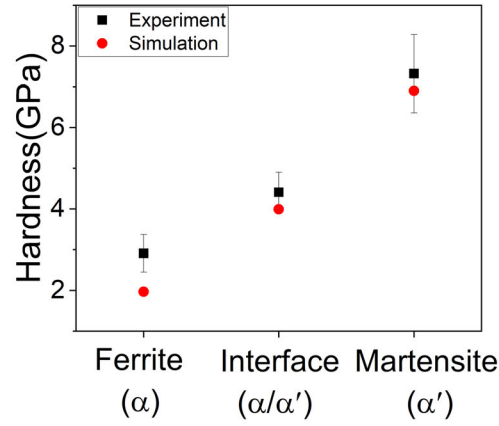
(b)
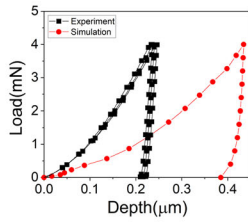
(c)   **(d)**   **(e)**

(f)

Fig 4. (a) FEM model showing location of indentation to determine ferrite, interface, and martensite hardness values. (b) Experimental and simulated hardness values for ferrite, interface, and martensite corresponding load–depth curves for (c) ferrite, (d) interface, (e) martensite, (f) plastic zone size versus maximum depth for all three indented locations.

plastic depth compared to the soft α phase, as expected. The novelty of this work is to demonstrate the ability to appropriately capture the PZS and shape in a micro-mechanical model that considers the actual microstructure of the DP steel, enabling their quantification and subsequent prediction of hardness for other volume fractions and hardness differentials in the composite structure.

Further, for a given load of 4 mN, the maximum depth corresponding to each indent is compared to the plastic zone underneath it in Fig. 4f to gauge the extent of the influence of the surrounding second phase on the measured hardness of the first. For a maximum depth h_{max} of 0.24 μm on martensite (marked as Martensite1 in Fig. 4a), the PZS is 0.53 μm. The indented martensite island has a particle size R of 2.5 μm, which corresponds to a normalized depth (ratio of maximum depth, h_{max}, to distance, d, from the ferrite–martensite interface) of 0.09 from the interface.

α' is usually a disconnected, sparsely distributed, irregularly shaped second phase, as shown in Fig. 1(a). Hence, there is lower probability that, in a matrix of indents, the indent falls exactly on the center of the α' island. In the eventuality that the indent is closer to the interface, the plastic zone will be influenced by the soft ferritic matrix around it, and hence a critical depth of indentation with respect to the island size and position is required to determine whether an indent is truly representative of the hardness of the individual phase.

Figure 5 shows the evolving plastic zone for an indent placed on an α' island at a distance of 0.8 μm from the interface (marked as "Martensite2" in Fig. 4a). It is irregularly shaped, especially when close to the interface, in contrast to the assumptions of an expanding hemispherical cavity which is assumed in homogeneous models. It can be seen from Fig. 5b that, with increasing values of maximum depth (h_{max}) normalized by distance to the ferrite–martensite interface (d), the hardness begins to decrease. This shows that erroneous values of martensite hardness would be obtained if the PZS is not appropriately taken into account, and if h_{max}/d exceeded 0.3. Hardness values for h_{max}/d values lower than 0.1 were not determined. as the PZS became finer than the mesh size. A well-developed plastic zone with a constant triaxiality ratio was ensured for all the indentation depths shown here, and smaller depths that would cause indentation size effects were not considered.

In a real nanoindentation experiment, the user would perform an array of indents with the same experimental parameters to phase-partition the data on such a microstructure. A correlative microscopy (via scanning electron microscopy images or EBSD) would help to reveal the distance of each indent from the ferrite–martensite interface. Hence, as observed from Fig. 5b, the user can ensure that the normalized depth (h_{max}/d) is below 0.30, such that interference from ferrite is negated. Therefore, the finite element model enables the differentiating
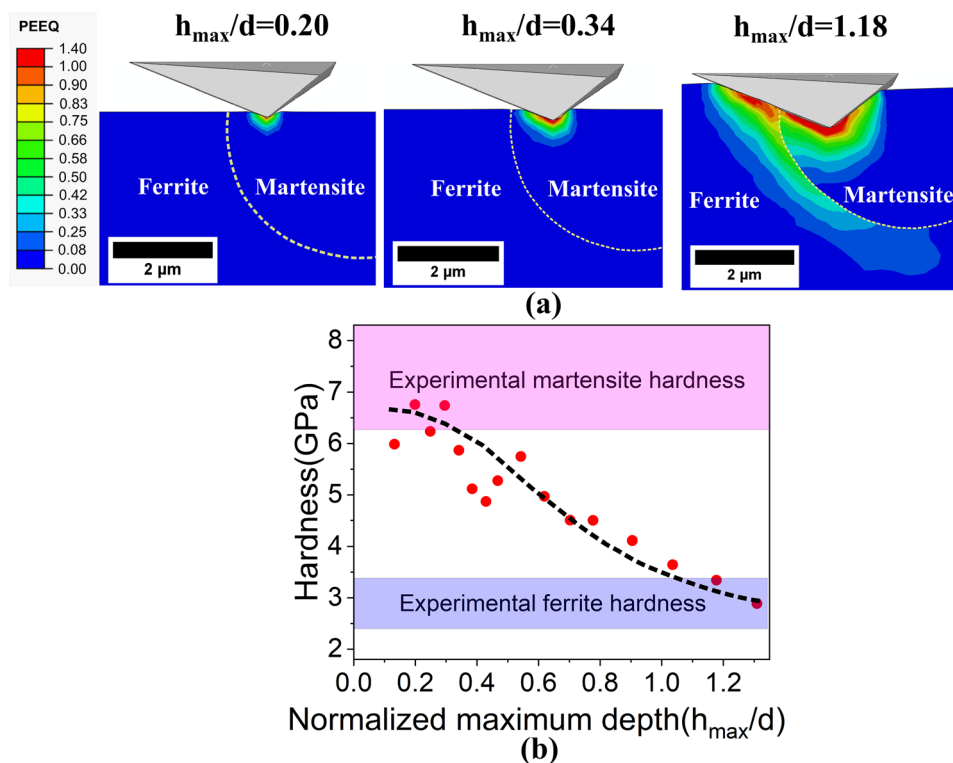

Fig 5. (a) Equivalent plastic strain contours for h_{max}/d of 0.20, 0.34, and 1.18, (b) hardness of martensite as function of normalized maximum depth.

of the information obtained from each indent, and finding the indent spacing in a phase-mapping experiment for a composite of hard–soft phases.

Effect of Tip Radius and Geometry on the Plastic Zone Size

This section compares and contrasts the effect of the tip geometry and tip radius on the PZS and the stress state on homogeneous substrates. These indentations have been simulated on single-phase martensite with load control at a maximum load of 10 mN. Figure 6a shows the PZS plotted as a function of depth for an ideally sharp Berkovich and a realistic tip with 100 nm radius. Both scale linearly with depth and show a PZS independent of the tip radius, confirming the constant strain nature of these tips. Further, the PZSs were calculated at a depth of ~200 nm (contact radius of 0.54 μm) for the Berkovich indenter. PZSs of 1.24 μm and 3.26 μm were obtained from Eqs. 1 and 2, respectively, while it was ~0.76 μm (measured in the vertical direction) from the simulated data.

In contrast, Fig. 6b shows the PZS as a function of spherical tips of different radii. This relationship is non-linear. There is a significant difference in PZS for a given depth at small radii, whereas the differences reduce at increasing radii. Naturally, a tip with a larger radius yields a larger plastic zone for a given depth, and has a steeply increasing PZS with increasing depth compared to those with smaller radii. When probing multi-phase composites such as DP steel, the choice of tip radii and indentation depth will depend on the feature size that is being probed, so as to ensure that the PZS is limited within the confines of the second-phase interface. A smaller tip radius is preferred when the feature size is small for recording the plastic response; however, a smaller radius also reduces the load and the corresponding depth required for elastic–plastic transition. At small depths, the indentation size effect will interfere with the

measurements. In addition, small irregularities in the shape of the indenter become amplified. For instance, the critical load at which elastic–plastic transition takes place is 0.02 mN for the 100-nm tip radius at a depth of ~7 nm, whereas it is 3.9 mN for the 50-μm tip radius at a depth of ~14 nm. In order to observe a clear elastic–plastic transition in a relatively soft material like DP steel, while maintaining the plastic zone confined to the individual martensite islands, a compromise at 10-μm tip radius would be ideal, which shows this transition to plasticity at ~0.2 mN. Figure 6b can then be used to determine the maximum depth to contain the plastic zone within the feature of interest in a composite structure. Finally, the choice of tip geometry and radius will also affect the h_{max}/d that can be employed in DP steels without interference from the second phase.

Effect of Intrinsic Properties of α' on the Plastic Zone Size

Upon tempering of DP steels, the hardness of the martensite decreases as expected, approaching that of the ferrite matrix. This corresponds to a lower yield strength and higher strain-hardening exponent in α'. Thus, the hardness differential ΔH is expected to come down (Fig. 2c), with the softer martensite expected to display a larger plastic zone, both of which are challenging for the objective of phase mapping. In this section, simulations were carried out on single-phase α' to decouple the influence of the yield strength (σ_{YS}) and strain-hardening exponent (n) on the PZS, to simulate the microstructures of tempered conditions. Three such cases were simulated, varying either the yield strength or the strain-hardening exponent separately using spherical indentation with a tip radius (R) of 10 μm (Fig. 7). It is clear that the PZS is a function of the yield strength, with an 80% decrease in yield strength increasing the PZS by ~46% for any applied depth (Fig. 7b, c). Thus, a thumb rule
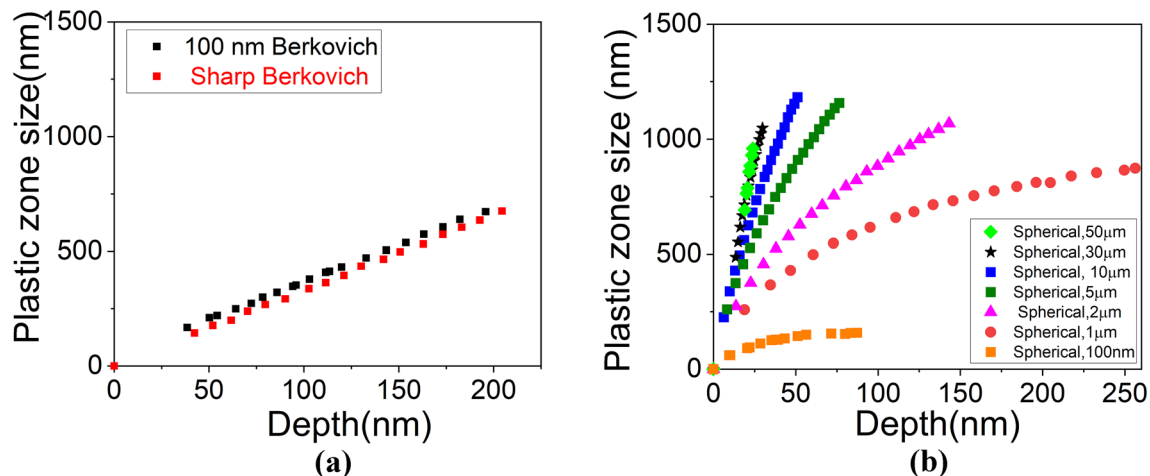

Fig 6. Plastic zone size as a function of depth for (a) Berkovich, and (b) spherical tips of different radii for the martensite phase.
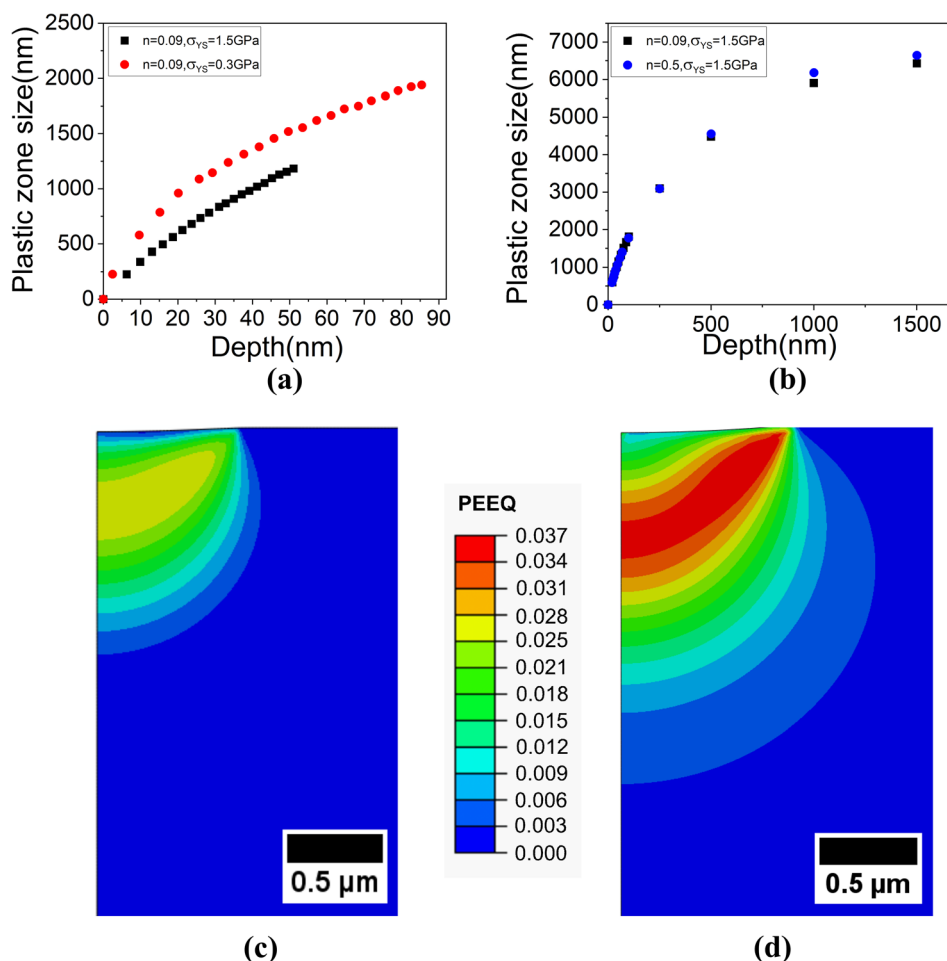
Fig 7. (a) Plastic zone size as a function of depth for different inputs, equivalent plastic strain (PEEQ) contours for (b) n = 0.09, YS = 1.5 GPa, (c) n = 0.09, YS = 0.3 GPa on single phase martensite at ~50 nm depth, where YS corresponds to the yield strength and *n* corresponds to the strain-hardening exponent.

separating the indents by 10 times the maximum depth may not always be valid, giving rise to overlapping plastic zones in the case of materials with low yield strengths. On the other hand, at the small depths and corresponding indentations strains ($a/R \leq 0.07$) simulated here, the strain-hardening exponent plays a negligible role, with the PZS remaining the same for a 200% increase in n. The difference in PZS becomes visible at larger applied strains, with a higher plastic zone occurring for a material with higher n. These are in accordance with other predictions in the literature, which have been made using Berkovich indentations.[24,56] However, since the applied strains in spherical indentations are smaller than for the sharp Berkovich tips for a given indentation depth, and the yield strength at which the n values are varied is high, the differences appear smaller than that reported in the literature.

The range of yield strength and n values used here covers the extreme ends of the spectrum of yield and strain-hardening characteristics of martensite subjected to tempering treatment.

Therefore, Fig. 7 can also be used to derive the h_{max}/d for the heat-treated DP steels, which will differ from the DP 600 that was employed in section "Hardness Measurements through Berkovich Indentations on Individual Phases".

Prediction of Composite Hardness in DP Steels for Varying Volume Fraction of α' and Hardness Differentials, and Experimental Comparison

The last objective of the study is to predict the hardness of the composite structure through a 3D model of DP steel at varying volume fractions of α' and hardness differentials ΔH, followed by comparison the with experimentally measured microhardness values. These mimic the microstructures obtained by different thermo-mechanical processes of inter-critical annealing and tempering. Figure 8a shows the simulated *P–h* response from Vickers indentation for all the microstructures together under a constant load of 100 mN. These lead to varying maximum depths based on the overall

(a)

(b)

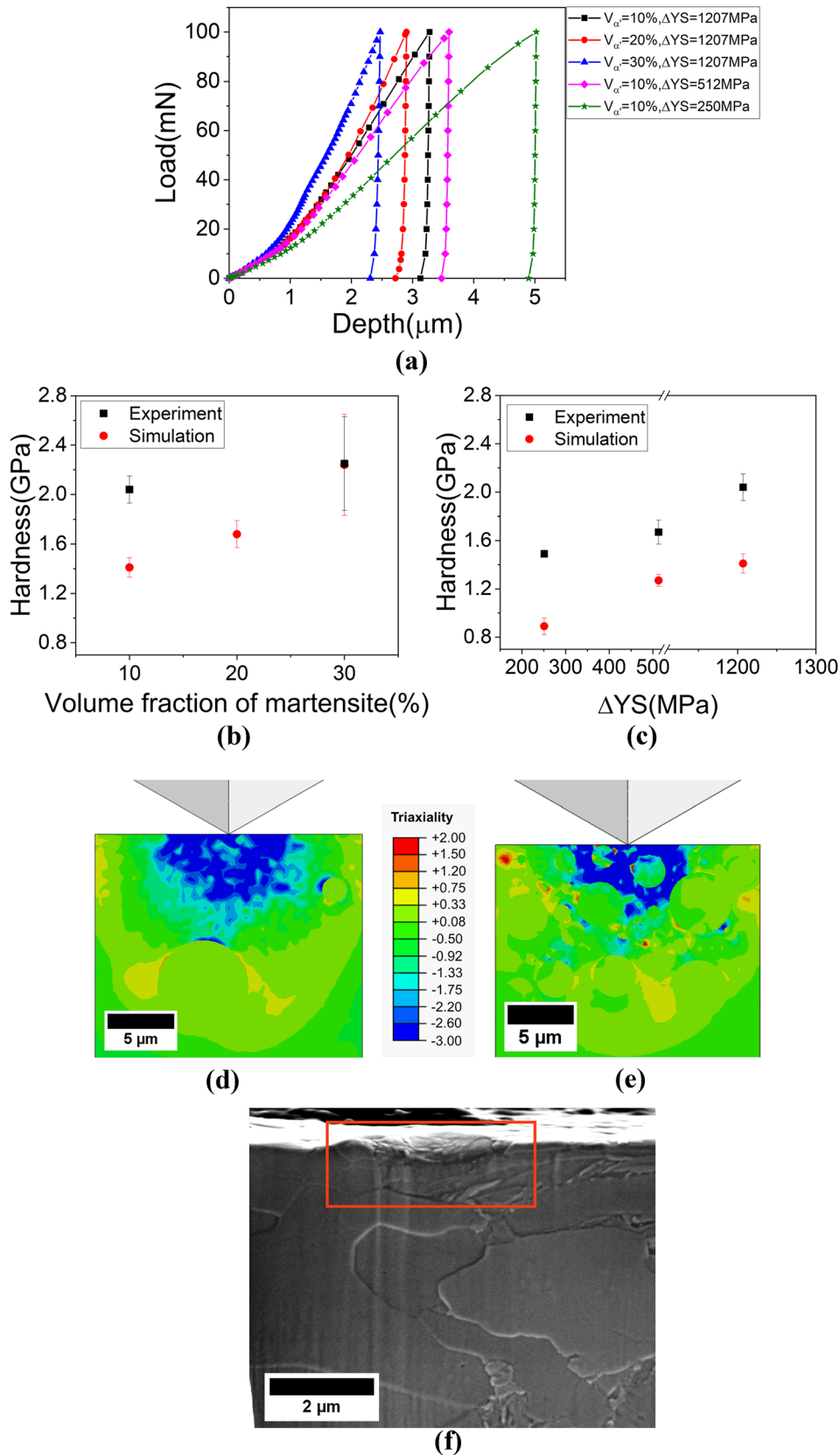
(c)

(d)

(e)

(f)

Fig 8. (a) Simulated load–depth responses for all cases of simulation, hardness obtained from simulations, and Vickers hardness measurements for different (b) volume fractions of martensite for ΔYS = 1207 MPa, (c) strength differentials in DP for $V_{\alpha'}$ = 10%, stress triaxiality contours for (d) $V_{\alpha'}$ = 10%, and (e) $V_{\alpha'}$ = 30% at ΔYS = 1207 MPa, (f) cross-section underneath a Vickers indent (*red box*) showing the features of an actual microstructure of DP steel participating in the plastic zone (Color figure online).

composite hardness. Due to the statistical nature of the distribution of the second phase, in this case most indents happened to be located on the ferritic matrix. The hardness is seen to follow a rule of mixtures with respect to the volume fraction of α' ($V_{\alpha'}$), increasing with increasing the α' fraction for a given ΔYS ($YS_{\alpha'}$–YS_{α}) of 1207 MPa (Fig. 8b). In addition, the composite hardness increases with increasing ΔYS for a given volume fraction of 10% (Fig. 8c). Both are expected. A lower $V_{\alpha'}$ and a lower ΔYS both lead to better (increasing) strain partitioning between the two phases, leading to higher strain accommodation and a larger plastic zone. For instance, the PZS in ferrite is found to be 5.9 ± 0.3 μm for the highest ΔYS condition and 7.2 ± 0.3 μm for the lowest ΔYS condition. While experimentally measured values are significantly different from the predicted ones, the relative changes are succinctly captured by the simulations. The PZS is an overestimation given that the microstructure is idealised assuming a spherical shape for all α' and a constant grain size for α, without incorporating an evolving dislocation structure under stain gradients and micro-residual stresses. However, this still allows us to gauge the mechanistic reasons for the observed trends.

Although a damage model was not built into the FEM in the present study, an idea of damage initiation and accumulation can be gathered from the stress triaxiality contour plots. Figure 8d, e shows the stress triaxiality across the indented cross-section for two different $V_{\alpha'}$, of 10% and 30%, at a constant ΔYS. While the magnitude of the triaxiality ratio is the same in both cases, the composite with a lower fraction of α' has a larger hydrostatically compressed zone, which implies delayed damage nucleation in it. The maximum positive triaxiality ratio is found to occur at the α–α' interface, while a smaller, yet positive, value occurs inside the α' islands. The position of the highest triaxiality ratio is an indicator of the location of damage initiation. Therefore, in DP steels, damage nucleation under indentation is expected to occur at the ferrite–martensite interface. It also implies that damage would initiate at smaller indentation depths for DP steels with higher $V_{\alpha'}$ and higher ΔYS. If the interface strengths are known, these plots can be utilized to predict the depth beyond which hardness measurements become invalid due to cracking/damage. Figure 8(f) reveals the microstructural features that participate in the plastic zone that develops underneath this composite structure. When the depth of penetration is about 2 μm, our simulation results predict a PZS in DP steel for a Vickers indentation to be about 10 μm. This plastic zone would extend to cover several ferrite grains and martensite islands, and result in damage evolution that cannot be captured using traditional models. In addition to the size distribution of the martensite islands, the morphology will also influence the plastic zone, but was not considered in the present study.

DISCUSSION

The present study uses virtual indentations through FEM to quantify the plastic zone evolution in DP steels, and to determine the effect of various geometric and microstructural parameters on the measured hardness. The primary focus of this work has been the determination of the nanoindentation properties of the hard martensite islands embedded in a soft ferritic matrix. This is not an effort towards optimization of the model to yield results close to those of the experiments, unlike in the works of Knapp et al.[11] or Karimzadeh et al.[10], but to just make relative comparisons of trends. This section contains two parts: (1) reasons for differences between simulated and experimental measurements of hardness, and (2) mechanistic understanding of the simulated indentation data and associated protocols for DP steels.

Figure 4b shows that the simulated measurements of hardness of individual phases is always lower than the experimentally measured values. While the former is measured from estimation of the indented area, in the latter, the conventional Oliver–Pharr method is used without any corrections. The tip geometry used in both cases is the same, including the tip radii. The Oliver–Pharr model is designed for homogeneous systems, and directly applying it into such heterogeneous microstructures may give rise to errors, especially when the surrounding matrix is softer than the phase being indented. However, the differences in the absolute values of hardness between the simulated and experimental data is primarily because of the idealisations of the microstructure in the simulations. Firstly, the simulated P–h responses have not been fit to the experimental P–h response by adjusting the input Rodriguez model, which results in the simulated loading curves having a significantly lower slope than the experimental curves. This indicates that the assumed yield strengths and strain-hardening behavior for the input maybe significantly different from the actual values, and need to be corrected for a direct correspondence in numbers. Unlike the loading segment, the unloading segment is primarily elastic, and hence shows a good correspondence between the experiments and the simulations. Secondly, the difference can be attributed to the pile-up, which was seen in the PEEQ contours of the indented cross-sections (e.g., Fig. 5a), which is not accounted for in the experiments due to the lack of post indentation imaging. A pile-up results in a larger actual area of indentation, and, if unaccounted, leads to overestimation of the hardness via the Oliver–Pharr method. While several correction factors have been given for single-phase materials with different extents of hardening, an analytical correction factor becomes challenging for a composite structure, and

therefore a numerical technique seems to be a better alternative. Thirdly, the microstructure is an idealised version of the real case, incorporating only the size distribution and not the shape distribution of α'. This will also have a significant bearing on the PZS, with an irregular α' giving a non-uniform plastic zone. There is definitely scope for improving the model to replicate the actual indentation curves to discern the individual effects separately. A more complex model closer to reality could be achieved through crystal plasticity,[57–59] wherein the individual grain-scale data from micropillar[49–52] experiments can be input into predicting the macro-indentation response of the material, as a few studies have done.[60,51] However, this is computationally intensive and was not within the scope of the present study.

Even with the above limitations, a normalized critical length scale is proposed in terms of indentation depth to feature the size ratio, to extract the properties of α' without interference from the ferritic matrix. Since both h_{max} and d are easily measurable quantities in an experiment, these have been used to develop this critical ratio. In addition, a relationship between the indentation depth and the PZS is proposed for various indenter tip radius, which can be coupled with the second-phase feature size, in this case α', to arrive at an optimum, such that the plastic zone is confined to the second phase alone. The fact that, even in the homogeneous case, the PZS obtained from our simulations is lower than that obtained from Eqs. 1 and 2 also shows that the elastic–perfectly plastic assumptions in the latter cause significant deviations from the actual behavior and cannot be directly employed in the case of DP steels. In addition to PZS, the location and severity of strain localization in the plastic zone is captured in the simulations (e.g., Figs 5a, 8d, e), which otherwise would require extensive experimental work. Severity of strain localization can be described by the maximum equivalent strain seen underneath the indenter for a given applied strain. For a fixed indentation depth of ∼240 nm using the Berkovich, it was seen that the martensite (with a higher yield strength and lower n) had a higher magnitude of maximum equivalent strain (0.84), although its PZS was smaller, while the ferrite (with a lower yield strength and higher n) had a lower maximum equivalent strain (0.51). Also, it was seen that, while spherical indents created a larger PZS, the severity of strain localization was an order of magnitude lower in them compared to a Berkovich for a fixed depth of the indentation.

More simulations are essential if the parameters identified in this study have to be used for generalized particulate composites. Incorporation of J2 plasticity and cohesive zone models will improve the accuracy with which the actual indentation response can be replicated and is being implemented. This requires capturing appropriate parameters for the input through micromechanical testing and will be carried out in a future work.

CONCLUSION

This study uses a micromechanical model of DP steel to determine the effect of extrinsic geometric parameters and a limited number of intrinsic microstructural parameters that affect the hardness measurements, primarily in the martensite, through finite element modeling. The basis for the quantification is the plastic zone, which is used to estimate the actual area of indentation. The evolution of the plastic zone is reflected in the differences in the hardness measured in the soft ferrite and hard martensite phases. The model correctly predicts the trend in hardness of the two-phase composite structure, as a function of the volume fraction of martensite and the hardness differential between the phases. More importantly, it allows for direct visualization of the plastic zone and stress triaxiality underneath the complex stress state, enabling the prediction of failure modes in these microstructures. A critical normalized depth to feature size ratio is determined, beyond which the measurements are influenced by the surrounding matrix phase in DP steels. This model therefore supplements the information obtained from an experiment without having to go through imaging of the indentations. It can also replace the more expensive process of locating and cross-sectioning the indents through site-specific micromachining tools to assess the damage zone under them. This model is a first step towards using more complex, grain-level finite element models to describe the indentation behavior of multi-phase composites that can capture their response more accurately.

CONFLICT OF INTEREST

On behalf of all authors, the corresponding author states that there is no conflict of interest.

APPENDIX 1

MICROSTRUCTURE INSTANTIATION

The random number generator module (RNG), as shown in Fig. 9, was developed using the Numpy library in the Python programming language, enabling the generation of random numbers required for input variables associated with the microstructure. In the present research, particle size distribution and Cartesian coordinates for

particle locations (x, y, z) were considered as these input variables. Particle sizes were sampled from the experimentally determined probability distribution, and the locations were uniformly distributed in all three directions. Using a defined routine, a new particle is added to the microstructure if it does not overlap with the existing particles. This process continues until the required reinforcement volume fraction is reached. The data generated from this module is sent to the customized FEA platform developed using the commercial software Abaqus/CAE v6.14 - 4® for model generation and analysis

sub-process. This FEA platform, shown in Fig. 10, was adopted using scripting in the Python programming language.

REFERENCES

1. J.B. Pethicai, R. Hutchings, and W.C. Oliver, *Philos. Mag. A Phys. Condens. Matter. Struct. Defects Mech. Prop.* 48, 593 (1983).
2. W.C. Oliver and G.M. Pharr, *J. Mater. Res.* 7, 1564 (1992).
3. B. Backes, K. Durst, and M. Göken, *Philos. Mag.* 86, 5541 (2006).
4. W.C. Oliver and G.M. Pharr, *J. Mater. Res.* 19, 3 (2004).
5. B. Merle, V. Maier, M. Göken, and K. Durst, *J. Mater. Res.* 27, 214 (2012).
6. M. Göken, M. Kempf, and W.D. Nix, *Acta Mater.* 49, 903 (2001).
7. Q. Furnémont, M. Kempf, P.J. Jacques, M. Göken, and F. Delannay, *Mater. Sci. Eng. A* 328, 26 (2002).
8. M. Delincé, P.J. Jacques, and T. Pardoen, *Acta Mater.* 54, 3395 (2006).
9. A. Bolshakov and G.M. Pharr, *J. Mater. Res.* 13, 1049 (1998).
10. A. Karimzadeh, M.R. Ayatollahi, and M. Alizadeh, *Comput. Mater. Sci.* 81, 595 (2014).
11. J.A. Knapp, D.M. Follstaedt, S.M. Myers, J.C. Barbour, and T.A. Friedmann, *J. Appl. Phys.* 85, 1460 (1999).
12. W. Yan, C.L. Pun, and G.P. Simon, *Compos. Sci. Technol.* 72, 1147 (2012).
13. K.L. Johnson, *J. Mech. Phys. Solids* 18, 115 (1970).
14. M. Yoshioka, *J. Appl. Phys.* 76, 7790 (1994).
15. W.W. Gerberich, D.E. Kramer, N.I. Tymiak, A.A. Volinsky, D.F. Bahr, and M.D. Kriese, *Acta Mater.* 47, 4115 (1999).
16. Y.L. Chiu and A.H.W. Ngan, *Acta Mater.* 50, 2677 (2002).
17. Y. Huang, S. Qu, K.C. Hwang, M. Li, and H. Gao, *Int. J. Plast.* 20, 753 (2004).
18. C.L. Woodcock and D.F. Bahr, *Scr. Mater.* 43, 783 (2000).
19. P. Chadwick, *Q. J. Mech. Appl. Math.* 12, 52 (1959).
20. D. Durban and N.A. Fleck, *J. Appl. Mech. Trans. ASME* 64, 743 (1997).
21. S.S. Chiang, D.B. Marshall, and A.G. Evans, *J. Appl. Phys.* 53, 298 (1982).
22. D. Bigoni and F. Laudiero, *Int. J. Mech. Sci.* 31, 825 (1990).
23. J. Lubliner, in *Plast. Theory* (Pearson Education,Inc., California, 1992), pp. 245–246.
24. M. Mata and O. Casals, *J. Alcala* 43, 5994 (2006).
25. J. Chen and S.J. Bull, *Surf. Coat. Technol.* 201, 4289 (2006).
26. J. Chen and S.J. Bull, *J. Mater. Res.* 21, 2617 (2006).
27. C.S. Han, H. Gao, Y. Huang, and W.D. Nix, *J. Mech. Phys. Solids* 53, 1188 (2005).
28. H. Gao, Y. Huang, W.D. Nix, and J.W. Hutchinson, *J. Mech. Phys. Solids* 47, 1239 (1999).
29. W.D. Nix and H. Gao, *J. Mech. Phys. Solids* 46, 411 (1998).
30. W. Yang, B.C. Larson, G.M. Pharr, G.E. Ice, J.D. Budai, J.Z. Tischler, and W. Liu, *J. Mater. Res.* 19, 66 (2004).
31. G. Feng, A.S. Budiman, W.D. Nix, N. Tamura, and J.R. Patel, *J. Appl. Phys.* 104, 043501 (2008).
32. D. Kiener, R. Pippan, C. Motz, and H. Kreuzer, *Acta Mater.* 54, 2801 (2006).
33. E. Demir, D. Raabe, N. Zaafarani, and S. Zaefferer, *Acta Mater.* 57, 559 (2009).
34. J.W. Kysar, Y.X. Gan, T.L. Morse, X. Chen, and M.E. Jones, *J. Mech. Phys. Solids* 55, 1554 (2007).
35. C.F.O. Dahlberg, Y. Saito, M.S. Öztop, and J.W. Kysar, *Int. J. Plast.* 54, 81 (2014).
36. S. Janakiram, P.S. Phani, G. Ummethala, S.K. Malladi, J. Gautam, and L.A.I. Kestens, *Scr. Mater.* 194, 113676 (2021).
37. E.D. Hintsala, U. Hangen, and D.D. Stauffer, *Jom* 70, 494 (2018).
38. J. Li, G. Dehm, and C. Kirchlechner, *Materialia* 7, 100378 (2019).
39. P.S. Phani and W.C. Oliver, *Mater. Des.* 164, 107563 (2019).
40. L.E. Samuels and T.O. Mulhearn, *J. Mech. Phys. Solids* 5, 125 (1957).
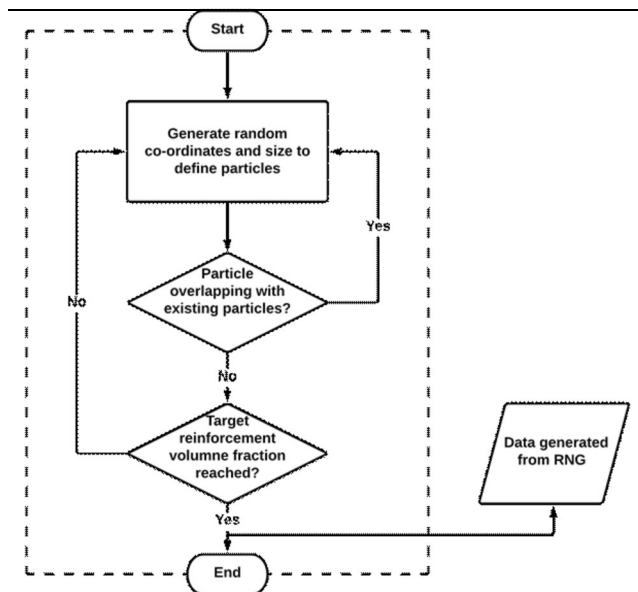
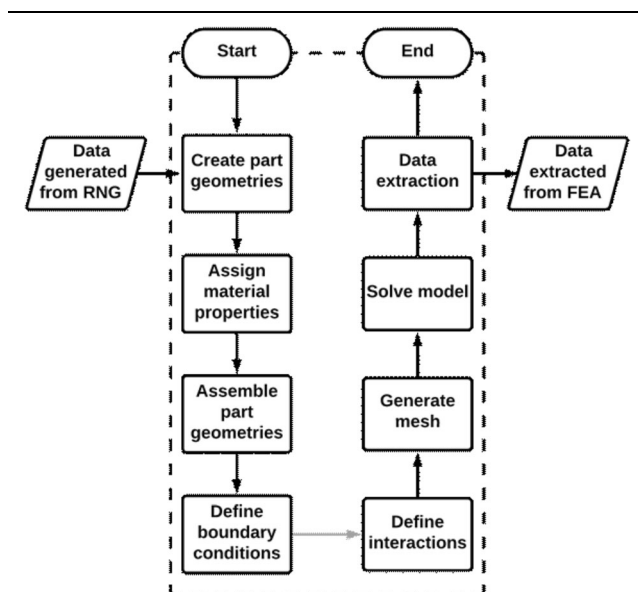Fig 9. Schematic of the random number generator (RNG) module.

Fig 10. Schematic of model generation and analysis of sub-process using the FEA platform.

41. ASTM Stand. **E92**, 1 (2017).
42. T. Matsuno, R. Ando, N. Yamashita, H. Yokota, K. Goto, and I. Watanabe, *Int. J. Mech. Sci.* 180, 105663 (2020).
43. J. Kadkhodapour, S. Schmauder, D. Raabe, S. Ziaei-Rad, U. Weber, and M. Calcagnotto, *Acta Mater.* 59, 4387 (2011).
44. S. Basu, N. Jaya, A. Patra, S. Ganguly, M. Dutta, A. Hohenwarter, and I. Samajdar, *Metall. Mater. Trans. A* 52A, 21 (2021).
45. S. Basu, A. Patra, B. . Jaya, S. Ganguly, M. Dutta, and I. Samajdar, in *14TH World Congr. Comput. Mech.* (2020).
46. A.C. Fischer-Cripps, *Nanoindentation*, 3rd edn. (Springer, Berlin, 2004).
47. R. Rodriguez and I. Gutierrez, *Mater. Sci. Forum* 426–432, 4525 (2003).
48. C. Du, F. Maresca, M.G.D. Geers, and J.P.M. Hoefnagels, *Acta Mater.* 146, 314 (2018).
49. C. Tian, D. Ponge, L. Christiansen, and C. Kirchlechner, *Acta Mater.* 183, 274 (2020).
50. C. Tian, G. Dehm, and C. Kirchlechner, *Materialia* 15, 100983 (2021).
51. P. Chen, H. Ghassemi-Armaki, S. Kumar, A. Bower, S. Bhat, and S. Sadagopan, *Acta Mater.* 65, 133 (2014).
52. H. Ghassemi-Armaki, R. Maaß, S.P. Bhat, S. Sriram, J.R. Greer, and K.S. Kumar, *Acta Mater.* 62, 197 (2014).
53. G.M. Pharr and W.C. Oliver, *J. Mater. Res.* 7, 613 (1992).
54. I.N. Sneddon, *Int. J. Engng Sci.* 3, 47 (1965).
55. R. Rodríguez and I. Gutierrez, *Mater. Sci. Eng. A* 361, 377 (2003).
56. Z. Yuan, Y. Wang, W. Tian, Y. Wang, K. Wang, F. Li, Y. Guo, Y. Hu, and X. Wang, *Philos. Mag. Lett.* 98, 209 (2018).
57. S.H. Choi, E.Y. Kim, W. Woo, S.H. Han, and J.H. Kwak, *Int. J. Plast.* 45, 85 (2013).
58. R.K. Verma and P. Biswas, *Mater. Sci. Technol. (United Kingdom)* 32, 1553 (2016).
59. M. Jafari, S. Ziaei-Rad, N. Saeidi, and M. Jamshidian, *Mater. Sci. Eng. A* 670, 57 (2016).
60. C.C. Tasan, M. Diehl, D. Yan, C. Zambaldi, P. Shanthraj, F. Roters, and D. Raabe, *Acta Mater.* 81, 386 (2014).